ANALYSIS AND TESTING FOR ROTORDYNAMIC COEFFICIENTS OF TURBULENT ANNULAR SEALS WITH DIFFERENT, DIRECTIONALLY HOMOGENEOUS SURFACE-ROUGHNESS TREATMENT FOR ROTOR AND STATOR ELEMENTS*

D. W. Childs and Chang-Ho Kim
Texas A&M University
College Station, Texas 77843

A combined analytical-computational method is developed to calculate the transient pressure field and dynamic coefficients for high-pressure annular seal configurations which may be used in interstage and neck-ring seals of multistage centrifugal pumps. The solution procedure applies to constant-clearance or convergent-tapered geometries which may have different (but directionally-homogeneous) surface-roughness treatments on the stator or rotor seal elements. It applies in particular to so-called "damper-seals" which employ smooth rotors and deliberately-roughened stator elements to enhance rotor stability.

Hirs' turbulent lubrication equations are modified slightly to account for different surface-roughness conditions on the rotor and stator. A perturbation analysis is employed in the eccentricity ratio to develop zeroth and first order perturbation equations. The zeroth-order equations define both the leakage and the development of circumferential flow due to shear forces at the rotor and stator surfaces. The first-order equations define perturbations in the pressure and axial and circumferential velocity fields due to small relative motion between the seal rotor and stator. The solution applies for small motion about a centered position and does not employ linearization with respect to either the taper angle or the degree of swirl, i.e., the difference between the circumferential velocity at the given axial position and the asymptotic circumferential-velocity solution.

Test results for four different surface-roughness confirm the predicted net damping increase for "damper seals". A round-hole-pattern stator yielded the highest net damping and lowest leakage of all seals tested. The seals are substantially stiffer than predicted, but the theory does an adequate job of predicting net damping.

NOMENCLATURE

a_i	Dimensionless coefficients defined in Appendix A
$\tilde{c}$, $\tilde{C}$	Dimensionless damping coefficients defined by Eq. (34)
$f(z)$	Dimensionless clearance function defined by Eq. (9)

*The results reported herein were partially supported by NASA Contract NAS8-33716 from the George C. Marshall Space Flight Center; Contract Monitor Frank Garcia.

$h(z) = H/\overline{C}$	Dimensionless clearance function
h_1	First-order perturbation clearance function defined by Eqs. (11) and (18)
$\tilde{k}$, $\tilde{K}$	Dimensionless seal stiffness coefficients defined by Eq. (34)
$\tilde{m}$, $\tilde{M}$	Dimensionless mass coefficients defined by Eq. (34)
ms, ns mr, nr	Dimensionless empirical turbulence coefficients for stator and rotor
p	Fluid pressure (F/L^2)
$\tilde{p} = p/\rho\overline{V}^2$	Dimensionless fluid-pressure introduced in Eq. (7)
$\tilde{p}_o$, $\tilde{p}_1$	Dimensionless fluid-pressure perturbations introduced in Eq. (11)
q	Taper-angle parameter defined in Eq. (10)
t	Independent variable time (T)
$u_Z = U_Z/\overline{V}$ $u_\theta = U_\theta/R\omega$	Dimensionless axial and circumferential velocity components introduced in Eq. (7)
$u_{\theta 0}$, $u_{\theta 1}$	Zeroth and first-order perturbations in u_θ
u_{Z0}, u_{Z1}	Zeroth and first-order perturbations in u_Z
$z = Z/L$	Dimensionless axial coordinate
A	Test orbit amplitude (L)
A_i	Dimensionless coefficients defined in Appendix A
$\overline{C}$	Nominal seal radial clearance, (L)
C_d	Seal discharge coefficients defined by Eq. (16)
C_0, C_1	Entrance and exit clearances, respectively, (L)
$H(z,\theta,t)$	Clearance function, illustrated in figure 2, and defined in Eq. (17), (L)
$H_o(z)$	Centered-clearance function defined by Eq. (9), (L)
L	Seal length (L)
P_s	Seal supply pressure (F/L^2)
ΔP	Nominal pressure-drop across seal (F/L^2)

R Seal radius (L)

$R_a = 2\rho VH/\mu$ Axial Reynolds number

$R_{ao} = 2\rho\overline{V}\overline{C}/\mu$ Centered-position, axial Reynolds number

$T = L/\overline{V}$ Transit time for a fluid element to traverse the seal

U_z, U_θ Axial and tangential bulk-flow fluid velocity components (L/T)

$V(z)$ Centered-position axial fluid velocity (L/T)

X, Y Radial seal displacements (L)

Z, $R\theta$ Spatial coordinates illustrated in Figure 2

α Seal taper angle illustrated in Figure 3

$\varepsilon = e/\overline{C}$ Seal eccentricity ratio introduced in Eq. (11)

$\hat{\varepsilon} = \hat{e}/2\overline{C}$ Relative roughness

ξ Inlet pressure-loss coefficient

λ_s, λ_r Dimensionless stator and rotor friction-factors defined in Eq. (15)

$\tau = t/T$ Dimensionless time

ω Shaft angular velocity (T^{-1})

Ω Shaft precessional velocity (T^{-1}), introduced in Eq. (22)

INTRODUCTION

Figure 1 illustrates the two seal types which have the potential for developing significant rotor forces. The neck or wear-ring seals are provided to reduce the leakage flow back along the front surface of the impeller face, while the interstage seal reduces the leakage from an impeller inlet back along the shaft to the backside of the preceding impeller. Pump seals may be geometrically similar to plain journal bearings, but typically have clearance to radius ratios on the order of 0.005 as compared to 0.001 for bearings. Because of the clearances, and normally-experienced pressure differentials, fully-developed turbulent flow normally exists in pump seals.

As related to rotordynamics, analysis of seals has the objective of defining the reaction force acting on a rotor as a consequence of shaft motion. For small motion about a centered position, the relation between the reaction-force components and shaft motion may be expressed by

$$-\begin{Bmatrix} F_x \\ F_y \end{Bmatrix} = \begin{bmatrix} K & k \\ -k & K \end{bmatrix} \begin{Bmatrix} x \\ y \end{Bmatrix} + \begin{bmatrix} C & c \\ -c & C \end{bmatrix} \begin{Bmatrix} \dot{x} \\ \dot{y} \end{Bmatrix} + \begin{bmatrix} M & m \\ -m & M \end{bmatrix} \begin{Bmatrix} \ddot{x} \\ \ddot{y} \end{Bmatrix} \tag{1}$$

The off-diagonal coefficients in Eq. (1) are referred to as "cross-coupled" and arise due to fluid rotation within the seal. Seals, unlike plain journal bearings, develop significant direct stiffness values K in the centered, zero-eccentricity position due to the distribution between (a) inlet losses, and (b) the axial pressure gradient due to wall-friction losses. Lomakin [1] initially pointed out the phenomenon. Both analysis [2] and experiments [3] have shown the Eq. (1) holds for fairly large eccentricies on the order of 0.5; i.e., the dynamic coefficients tend to be relatively insensitive to changes in the static-eccentricity ratio.

Prior analytical and experimental developments have generally examined "smooth" seals where both stator and rotor elements of the seal are assumed to have the same nominally smooth surfaces. A review of the analytical and experimental developments for this type of seal is provided in references [4] and [5] and will not be repeated here. The subject of this investigation is the so-called "damper-seal" configuration recently proposed by von Pragenau [6], which employs a smooth rotor and a deliberately surface-roughened stator element. For the same surface roughness on the rotor and stator, the asymptotic, circumferential, bulk-flow velocity is $R\omega/2$ in the centered position because (a) the radial velocity distribution is assumed to be symmetrical about the midplane, and (b) the circumferential velocity is zero at the stator wall and $R\omega$ at the rotor wall. Von Pragenau's analysis demonstrates that the damper seal yields a lower asymptotic circumferential velocity which implies a reduction in the destabilizing cross-coupled stiffness coefficient k and a consequential improvement in rotordynamic stability.

Von Pragenau employs an approximate "short-seal" analysis to develop analytical expressions for the rotordynamic coefficients of constant clearance seals. The development of these analytical expressions is lengthy and difficult. The combined analytical-computational approach used in this development yields an exact numerical solution to the governing equations for both constant-clearance and convergent-tapered seals with significantly less labor. Following a slight modification to Hirs' [7] governing equation to account for different surface-roughness conditions on the rotor and stator, the analysis procedure is ~~basically~~ that of reference [4] and [5].

GOVERNING EQUATIONS

Figure 2 illustrates a differential element of fluid having dimensions $Rd\theta$, dz, and $H\ (Z,\ \theta,\ t)$. The upper and lower surfaces of the element correspond to the rotor and stator seal elements and have velocities of $R\omega$ and zero, respectively. The bulk velocity components of the fluid are U_θ and U_z; i.e., these are the averages across the fluid film height H of the circumferential and axial fluid velocities. The essence of Hirs' formulation is the definition of the wall shear stress τ_w as the following empirical function of the bulk flow velocity V_w <u>relative</u> to the wall

$$\tau_w = \rho \frac{V_w^2}{2} no \left(\frac{2\rho V_w H}{\mu}\right)^{mo} = \rho \frac{V_w{}^2}{2} no\ R_a^{mo} \tag{2}$$

The bulk flow velocities relative to the rotor and stator are, respectively

$$\begin{aligned} \underline{V}_r &= (U_\theta - R\omega)\ \underline{\varepsilon}_\theta + U_z\ \underline{\varepsilon}_z \\ \underline{V}_s &= U_\theta \underline{\varepsilon}_\theta + U_z\ \underline{\varepsilon}_z \end{aligned} \tag{3}$$

Hence, the shear stress at the rotor and stator are

$$\tau_r = \rho \frac{V_r^2}{2} nr \left(\frac{2\rho V_r H}{\mu}\right)^{mr}$$
$$\tau_s = \rho \frac{V_s^2}{2} ns \left(\frac{2\rho V_s H}{\mu}\right)^{ms} \tag{4}$$

Hirs' formulation assumes that the surface roughness is the same on the stator and rotor; hence, the same empirical constants mo, no apply to both surfaces. The formulation of Eq. (4) accounts for different surface roughnesses in the seal elements via the empirical constants (mr, nr), (ms, ns) for the rotor and stator surfaces.

The components of wall shear surface stress in the Z and $R\theta$ directions are

$$\tau_{r\theta} = \tau_r \,(U_\theta - R\omega)\,/V_r; \; \tau_{rZ} = \tau_r \,U_Z/V_r$$
$$V_r = [(U_\theta - R\omega)^2 + U_Z^{\,2}]^{\frac{1}{2}}$$
$$\tau_{s\theta} = \tau_s \,U_\theta/V_s, \; \tau_{sZ} = \tau_s \,U_Z/V_s \tag{5}$$
$$V_s = (U_\theta^{\,2} + U_Z^{\,2})^{\frac{1}{2}}$$

Summing forces in the Z and $R\theta$ directions for the free-body diagram of figure 2 (b) yields the following momentum equations*:

$$-H \frac{\partial p}{\partial Z} = \frac{ns}{2} \rho U_Z^{\,2} R_a^{\,ms} \left[1 + (U_\theta/U_Z)^2\right]^{\frac{ms+1}{2}}$$
$$+ \frac{nr}{2} \rho U_Z^{\,2} R_a^{\,mr} \left\{1 + [(U_\theta - R\omega)/U_Z]^2\right\}^{\frac{mr+1}{2}} \tag{6a}$$
$$+ \rho H \left[\frac{\partial U_Z}{\partial t} + \frac{U_\theta}{R}\frac{\partial U_Z}{\partial \theta} + U_Z \frac{\partial U_Z}{\partial Z}\right]$$

$$-\frac{H}{R}\frac{\partial p}{\partial \theta} = \frac{ns}{2} \rho U_Z U_\theta R_a^{\,ms} \left[1 + (U_\theta/U_Z)^2\right]^{\frac{ms+1}{2}}$$
$$+ \frac{nr}{2} \rho U_Z (U_\theta - R\omega) R_a^{\,mr} \left\{1 + [(U_\theta - R\omega)/U_Z]^2\right\}^{\frac{mr+1}{2}} \tag{6b}$$
$$+ \rho H \left[\frac{\partial U_\theta}{\partial t} + \frac{U_\theta \partial U_\theta}{R\partial \theta} + U_Z \frac{\partial U_\theta}{\partial Z}\right]$$

The bulk-flow continuity equation is

$$\frac{\partial H}{\partial t} + \frac{1}{R}\frac{\partial (HU_\theta)}{\partial \theta} + \frac{\partial (HU_Z)}{\partial Z} = 0 \tag{6c}$$

*The continuity Eq. (6.c) has been used to simplify these momentum equations.

These equations may be nondimensionalized by introducing the following variables:

$$u_Z = U_Z/\overline{V}, \quad u_\theta = U_\theta/R\omega, \quad \tilde{p} = p/\rho\overline{V}^2$$

$$h = H/\overline{C}, \quad \tau = t/T, \quad z = Z/L \tag{7}$$

$$T = L/\overline{V}, \quad b = \overline{V}/R\omega$$

where $\overline{C}$ and $\overline{V}$ are the average clearance and axial velocity, respectively. The resultant equations are

$$\begin{aligned} -h\frac{\partial\tilde{p}}{\partial z} = {} & \frac{ns}{2}\left(\frac{L}{\overline{C}}\right) R_a^{\,ms}\left[1+\left(\frac{u_\theta}{bu_z}\right)^2\right]^{\frac{ms+1}{2}} u_z^{\,2} \\ & + \frac{nr}{2}\left(\frac{L}{\overline{C}}\right) R_a^{\,mr}\left[1+\left(\frac{u_\theta-1}{bu_z}\right)^2\right]^{\frac{mr+1}{2}} u_z^{\,2} \\ & + h\left[\frac{\partial u_z}{\partial\tau} + u_\theta(\omega T)\frac{\partial u_z}{\partial\theta} + u_z\frac{\partial u_z}{\partial z}\right] \end{aligned} \tag{8}$$

$$\begin{aligned} -b\left(\frac{L}{\overline{C}}\right) h\frac{\partial\tilde{p}}{\partial\theta} = {} & \frac{ns}{2}\left(\frac{L}{\overline{C}}\right) R_a^{\,ms}\left[1+\left(\frac{u_\theta}{bu_z}\right)^2\right]^{\frac{ms+1}{2}} u_z u_\theta \\ & + \frac{nr}{2}\left(\frac{L}{\overline{C}}\right) R_a^{\,mr}\left[1+\left(\frac{u_\theta-1}{bu_z}\right)^2\right]^{\frac{mr+1}{2}} u_z(u_\theta-1) \\ & + h\left[\frac{\partial u_\theta}{\partial\tau} + u_\theta(\omega T)\frac{\partial u_\theta}{\partial\theta} + u_z\frac{\partial u_\theta}{\partial z}\right] \end{aligned}$$

$$\frac{\partial h}{\partial\tau} + (\omega T)\frac{\partial(hu_\theta)}{\partial\theta} + \frac{\partial(hu_z)}{\partial z} = 0$$

PERTURBATION EQUATIONS

Seal Geometry

Figure 3 illustrates the geometry for a tapered seal. At the centered position, the clearance function is defined by

$$H_0(z) = (\overline{C} + \frac{\alpha L}{2}) - \alpha Z = [1 + q\ (1 - 2z)]\ \overline{C} = f\ \overline{C} \tag{9}$$

where α is the taper angle, and

$$\bar{C} = (C_0 + C_1)/2, \quad q = \frac{\alpha L}{2\bar{C}} = \frac{C_0 - C_1}{C_0 + C_1} \tag{10}$$

The parameter q is a measure of the degree of taper in a seal and varies from zero, for a constant-clearance configuration, to approximately 0.4 for a maximum-stiffness seal design [8].

Perturbation Analysis

The governing Eqs. (6) define the bulk-flow velocity components (u_θ, u_z) and the pressure, p, as a function of the spatial variables ($R\theta$, z) and time, t. An expansion of these equations in the perturbation variables

$$\begin{aligned} u_z &= u_{z0} + \varepsilon\, u_{z1}, \quad h = h_0 + \varepsilon\, h_1 \\ u_\theta &= u_{\theta 0} + \varepsilon\, u_{\theta 1}, \quad \tilde{p} = \tilde{p}_0 + \varepsilon\, \tilde{p}_1 \end{aligned} \tag{11}$$

where $\varepsilon = e/\bar{C}$ is the eccentricity ratio yields the following equations:

Zeroth-Order Equations:

(a) Axial-Momentum Equation

$$\frac{d\tilde{p}_0}{dz} = -\left[(a_{0s}\sigma_s + a_{0r}\,\sigma_r) + 4q\right]/2f^3 \tag{12a}$$

(b) Circumferential-Momentum Equation

$$\frac{du_{\theta 0}}{dz} = -\left[a_{0r}\,\sigma_r(u_{\theta 0} - 1) + a_{0s}\,\sigma_s\,u_{\theta o}\right]/2f \tag{12b}$$

(c) Continuity Equation

$$u_{z0} = 1/f \tag{12c}$$

First-Order Equations

(a) Axial-Momentum Equation

$$\begin{aligned} \frac{\partial \tilde{p}_1}{\partial z} &= h_1 A_{1z} - u_{\theta 1} A_{2z} - u_{z1} A_{3z} \\ &\quad - \left\{\frac{\partial u_{z1}}{\partial \tau} + (\omega T)\, u_{\theta 0}\frac{\partial u_{z1}}{\partial \theta} + \frac{1}{f}\frac{\partial u_{z1}}{\partial z}\right\} \end{aligned} \tag{13a}$$

(b) Circumferential-Momentum Equation

$$b\left(\frac{L}{R}\right)\frac{\partial \tilde{p}_1}{\partial \theta} = h_1 A_{1\theta} - u_{\theta 1} A_{2\theta} - u_{z1} A_{3\theta} - \left\{ \frac{\partial u_{\theta 1}}{\partial \tau} + (\omega T)\, u_{\theta 0} \frac{\partial u_{\theta 1}}{\partial \theta} + \frac{1}{f}\frac{\partial u_{\theta 1}}{\partial z} \right\} \tag{13b}$$

(c) Continuity Equation

$$\frac{\partial u_{z1}}{\partial z} + (\omega T)\frac{\partial u_{\theta 1}}{\partial \theta} - \frac{2q}{f} u_{z1} = -\frac{1}{f}\left[\frac{2qh_1}{f^2} + (\omega T)\, u_{\theta 0}\frac{\partial h_1}{\partial \theta} + \frac{\partial h_1}{\partial \tau}\right] \tag{13c}$$

Most of the parameters of these equations are defined in Appendix A. The quanities σ_s, σ_r are defined by

$$\sigma_s = \left(\frac{L}{\bar{C}}\right)\lambda_s,\ \sigma_r = \left(\frac{L}{\bar{C}}\right)\lambda_r \tag{14}$$

where the wall friction factors are defined by

$$\lambda_s = nsR_{a0}^{ms}\left(1 + \frac{1}{4b^2}\right)^{\frac{1+ms}{2}},\quad \lambda_r = nrR_{a0}^{mr}\left(1 + \frac{1}{4b^2}\right)^{\frac{1+mr}{2}} \tag{15}$$

These expressions correspond to Yamada's [9] test correlation for flow between rotating annulli.

SOLUTION PROCEDURES

Zeroth-Order Equations

The zeroth-order equations define the steady-state leakage and the circumferential velocity development $u_{\theta 0}$ (z) due to wall shear. The governing equations, Eqs. (12), are coupled and nonlinear through the dependency of the coefficients a_{0r}, a_{0s}, $u_{\theta 0}$ and $\bar{V}$. The equations must be solved iteratively to determine the average leakage velocity $\bar{V}$ corresponding to a specified pressure drop ΔP and the circumferential velocity distribution $u_{\theta 0}$ (z). The resultant solution defines the leakage coefficient C_d of the leakage ΔP relationship

$$\Delta P = C_d \frac{\rho \bar{V}^2}{2} \tag{16}$$

The pressure drop at the entrance is defined by

$$\Delta P_0 = \frac{\rho \bar{V}^2}{2}\ \frac{(1+\xi)}{(1+q)^2}$$

where ξ is an entrance-loss coefficient which is generally on the order of 0.1 to 0.5.

First-Order Equations

The governing first-order equations define $p_1(z, \theta, \tau)$, u_{z1} (z, θ, τ), and $u_{\theta 1}$ (z, θ, τ) resulting from the seal clearance functions h_1 (θ, τ). The clearance H is defined in terms of the components of the seal-journal displacement vector (X, Y) by

$$H = H_0 - X \cos\theta - Y \sin\theta \tag{17}$$

Hence, by comparison to Eq. (11),

$$\varepsilon h_1 = -x \cos\theta - y \sin\theta \tag{18}$$

where

$$x = X/\bar{C}, \quad y = Y/\bar{C}$$

Note that h_1 is not a function of z, and its time dependency arises from the displacement variables x (t), y (t).

To satisfy circumferential continuity conditions, the following solution format is assumed:

$$\begin{aligned} u_{z1}\,(z, \theta, \tau) &= u_{z1C}\,(z, \tau) \cos\theta + u_{z1s}\,(z, \tau) \sin\theta \\ u_{\theta 1}\,(z, \tau, \theta) &= u_{\theta 1C}\,(z, \tau) \cos\theta + u_{\theta 1s}\,(z, \tau) \sin\theta \\ \tilde{p}_1\,(z, \theta, \tau) &= \tilde{p}_{1C}\,(z, \tau) \cos\theta + \tilde{p}_{1s}\,(z, \tau) \sin\theta \end{aligned} \tag{19}$$

Substituting from Eq. (19) into Eq. (13) eliminates θ as an independent variable, and yields six real equations. By introducing the complex variables

$$\begin{aligned} \hat{u}_{z1} &= u_{z1C} + j u_{z1s} \\ \hat{u}_{\theta 1} &= u_{\theta 1C} + j u_{\theta 1s} \\ \tilde{p}_1 &= \tilde{p}_{1C} + j \tilde{p}_{1s} \\ \frac{\hat{h}_1}{\varepsilon} &= \frac{x}{\varepsilon} + j \frac{y}{\varepsilon} \end{aligned} \tag{20}$$

into these equations, the following complex equations are obtained

$$\begin{aligned} -\frac{\partial \hat{p}_1}{\partial z} &= A_{1z} \left(\frac{\hat{h}_1}{\varepsilon}\right) + A_{2z}\, \hat{u}_{\theta 1} + A_{3z}\, \hat{u}_{z1} \\ &\quad + \frac{\partial \hat{u}_{z1}}{\partial \tau} - j\,(\omega T)\, u_{\theta 0}\, \hat{u}_{z1} + \frac{1}{f} \frac{\partial \hat{u}_{z1}}{\partial z} \\ j\, b \left(\frac{L}{R}\right) \hat{p}_1 &= A_{1\theta} \left(\frac{\hat{h}_1}{\varepsilon}\right) + A_{2\theta}\, \hat{u}_{\theta 1} + A_{3\theta}\, \hat{u}_{z1} \\ &\quad + \frac{\partial \hat{u}_{\theta 1}}{\partial \tau} - j\,(\omega T)\, u_{\theta 0}\, \hat{u}_{\theta 1} + \frac{1}{f} \frac{\partial \hat{u}_{\theta 1}}{\partial z} \end{aligned} \tag{21}$$

$$\frac{\partial \hat{u}_{z1}}{\partial z} - j\,(\omega T)\,\hat{u}_{\theta 1} - \frac{2q}{f}\hat{u}_{z1} = \frac{2q}{f^3}\left(\frac{\hat{h}_1}{\varepsilon}\right) - j\,\frac{(\omega T)}{f}\,u_{\theta o}\left(\frac{\hat{h}_1}{\varepsilon}\right) + \frac{1}{f}\frac{\partial}{\partial \tau}\left(\frac{\hat{h}_1}{\varepsilon}\right)$$

with the A_i coefficients defined in Appendix A. The time dependency in these equations is eliminated by assuming a harmonic seal motion of the form

$$\hat{h}_1 = \frac{R_0}{\bar{C}}\ e^{j\Omega t} = r_0 e^{j\Omega T\tau} \tag{22}$$

where r_0 is a real constant. The associated harmonic solution can then be stated

$$\begin{aligned} \hat{u}_{z1}\ (z,\ \tau) &= \bar{u}_{z1}\ (z)\ e^{j\Omega T\tau} \\ \hat{u}_{\theta 1}\ (z,\ \tau) &= \bar{u}_{\theta 1}\ (z)\ e^{j\Omega T\tau} \\ \hat{p}_1\ (z,\ \tau) &= \bar{p}_1\ (z)\ e^{j\Omega T\tau} \end{aligned} \tag{23}$$

Substitution from Eqs. (22) and (23) into Eq. (21) yields

$$\frac{d}{dz}\begin{Bmatrix} \bar{u}_{z1} \\ \bar{u}_{\theta 1} \\ \bar{p}_1 \end{Bmatrix} + [A]\begin{Bmatrix} \bar{u}_{z1} \\ \bar{u}_{\theta 1} \\ \bar{p}_1 \end{Bmatrix} = \left(\frac{r_0}{\varepsilon}\right)\begin{Bmatrix} g_1 \\ g_2 \\ g_3 \end{Bmatrix} \tag{24}$$

where

$$[A] = \begin{bmatrix} -2q/f & -j\,(\omega T) & 0 \\ fA_{3\theta} & f\,(A_{2\theta}+j\Gamma T) & -jfb\,(L/R) \\ (A_{3z}+2q/f^2+j\Gamma T) & A_{2z}+j\,(\omega T)/f & 0 \end{bmatrix} \tag{25a}$$

$$\begin{Bmatrix} g_1 \\ g_2 \\ g_3 \end{Bmatrix} = \begin{Bmatrix} (2q/f^3+j\Gamma T/f) \\ -fA_{1\theta} \\ -(A_{1z}+2q/f^4+j\Gamma T/f^2) \end{Bmatrix} \tag{25b}$$

and

$$\Gamma = \Omega - \omega u_{\theta 0}(z) \tag{26}$$

The following three boundary conditions are specified for the solution of Eq. (24):

(a) The exit pressure perturbation is zero; i.e.,

$$\bar{p}_1(L) = 0 \tag{27}$$

(b) The entrance circumferential velocity perturbation is zero; i.e.,

$$\bar{u}_{\theta 1}(0) = 0 \tag{28}$$

(c) The pressure loss at the seal entrance is defined by

$$p_s - p(0, \theta, \tau) = \frac{\rho}{2} u_z^{\,2}(0, \theta, \tau)\ (1 + \xi)$$

which yields the following boundary condition:

$$\bar{p}_1(0) = -\ (1 + \xi)\ u_{z1}(0)/(1+q) \tag{29}$$

Solution of the differential Eqs. (24) in terms of the boundary conditions is relatively straightforward, yielding a solution for the velocity and pressure fields of the form

$$\begin{Bmatrix} \bar{u}_{z1} \\ \bar{u}_{\theta 1} \\ \bar{p}_1 \end{Bmatrix} = \left(\frac{r_o}{\varepsilon}\right) \begin{Bmatrix} f_{1C}+jf_{1s} \\ f_{2C}+jf_{2s} \\ f_{3C}+jf_{3s} \end{Bmatrix} \tag{30}$$

Dynamic Coefficient Definitions

Having obtained the pressure-field solution of Eq. (30), solution for the dynamic coefficients will now be undertaken. The reaction-force components acting on the rotor due to shaft motion are defined by

$$F_X(t) = -\varepsilon RL \int_o^1 \int_o^{2\pi} p_1 \cos\theta d\theta dz = -\varepsilon RL\rho\bar{V}^2 \int_o^1 \int_o^{2\pi} \tilde{p}_1 \cos\theta d\theta dz$$

$$F_Y(t) = -\varepsilon RL \int_o^1 \int_o^{2\pi} p_1 \sin\theta d\theta dz = -\varepsilon RL\rho\bar{V}^2 \int_o^1 \int_o^{2\pi} \tilde{p}_1 \sin\theta d\theta dz$$

From the last of Eq. (19), these integrals further reduce to

$$F_X(t) = -\varepsilon RL\pi\rho\bar{V}^2 \int_o^1 \tilde{p}_{1C} dz;\ F_Y(t) = -\varepsilon RL\pi\rho\bar{V}^2 \int_o^1 \tilde{p}_{1s} dz \tag{31}$$

The motion defined by Eq. (22) is orbital at the precessional frequency Ω and radius R_o. This statement may be confirmed by comparing Eq. (18) with Eq. (22) to obtain

$$X = \bar{C}r_o \cos\Omega t, \qquad Y = \bar{C}r_o \sin\Omega t \tag{32}$$

Definition of the reaction forces is simplified by performing the integration at a time when the rotating displacement vector is pointing along the X axis, i.e., when $\Omega t = 0$. Eq. (23) shows that $\hat{p}_1$ and $\bar{p}_1$ coincide for this time and location. Hence, Eq. (31) yields the following component force definitions parallel and normal to the displacement vector

$$F_r(\Omega T) = -r_o(\pi RL\rho\bar{V}^2) \int_o^1 f_{3C}(z)dz$$

$$F_\theta(\Omega T) = -r_o(\pi R L \rho \bar{V}^2) \int_o^1 f_{3s}(z)dz$$

The useful nondimensional version of these equations is

$$\frac{F_r(\Omega T)}{\pi R \Delta P R_o} = -\frac{2}{C_d} \frac{L}{\bar{C}} \int_o^1 f_{3c}(z)dz$$

$$\frac{F_\theta(\Omega T)}{\pi R \Delta P R_o} = -\frac{2}{C_d} \frac{L}{\bar{C}} \int_o^1 f_{3s}(z)dz \tag{33}$$

where $R_o = \bar{C}r_o$ is the amplitude of seal motion. The components are expressed as function of ΩT, because, for a given seal geometry (L, R, C) and set of operating conditions (ΔP, ω), the excitation frequency ΩT is the only independent variable. Stated differently, Eq. (33) provides a frequency-response solution for the reaction force components.

To calculate seal coefficients, a comparable statement of reaction-force components is developed from the following nondimensional statement of Eq. (1)

$$-\frac{1}{\pi R \Delta P}\begin{Bmatrix} F_X \\ F_Y \end{Bmatrix} = \begin{bmatrix} \tilde{K} & \tilde{k} \\ -\tilde{k} & \tilde{K} \end{bmatrix}\begin{Bmatrix} X \\ Y \end{Bmatrix} + T\begin{bmatrix} \tilde{C} & \tilde{c} \\ -\tilde{c} & \tilde{C} \end{bmatrix}\begin{Bmatrix} \dot{X} \\ \dot{Y} \end{Bmatrix} + T^2\begin{bmatrix} \tilde{M} & \tilde{m} \\ -\tilde{m} & \tilde{M} \end{bmatrix}\begin{Bmatrix} \ddot{X} \\ \ddot{Y} \end{Bmatrix} \tag{34}$$

Substitution from Eq. (32) yields

$$-\frac{F_r(\Omega T)}{\pi R \Delta P R_o} = \tilde{K} + \tilde{c}(\Omega T) - \tilde{M}(\Omega T) = \frac{+2}{C_d}\left(\frac{L}{\bar{C}}\right) \int_o^1 f_{3c}(z)dz$$

$$\frac{F_\theta(\Omega T)}{\pi R \Delta P R_o} = \tilde{k} - \tilde{C}(\Omega T) - \tilde{m}(\Omega T) = \frac{-2}{C_d}\left(\frac{L}{\bar{C}}\right) \int_o^1 f_{3s}(z)dz \tag{35}$$

Hence, the dynamic seal coefficients (K, k, C, c, M, m) may be obtained by comparing the solution obtained by Eq. (33) with Eq. (35). More specifically, they are obtained by a least-square curve-fit of the solutions stated on the right-hand side of Eq. (35).

TANGENTIAL VELOCITY DEVELOPMENT

The frames of figure 4 illustrate the circumferential velocity development $u_{\theta o}(z)$ which is predicted by Eq. (12b) for the same and different rotor and stator surface roughnesses. Roughness is characterized by the empirical coefficients (mr, nr), (ms, ns). For the figures illustrated, the roughness of a smooth surface is defined by Yamada's [9] coefficients

$$mo = -0.25, \qquad no = 0.079$$

while the parameters

$$mo = -.0024, \qquad no = 0.0262,$$

corresponding to a theoretical relative roughness $\hat{\epsilon} = \hat{e}/2\bar{C} = 0.1$ are used for the rough surface. Observe that the solution converges towards one half irrespective of whether both surfaces are smooth or rough. However, in figure 4 (b) the asymptotic solution is less or greater than one half depending on whether one uses a smooth-rotor/rough-stator or a rough-rotor/smooth-stator combination. The results of figure 4 substantially support von Pragenau's [6] central conclusion concerning the desirability of a rough-stator/smooth-rotor combination.

EXPERIMENTAL RESULTS

Introduction

The test results reported here were developed as part of an extended, NASA-funded, high-Reynolds-number test program of pump seal configurations in support of the SSME (Space Shuttle Main Engine) development program. High-Reynolds numbers, which are comparable to those achieved in the cryogenic turbopumps of the SSME, are achieved by using $CBrF_3$ as a test fluid. This is a DuPont-manufactured refrigerent and fire extinguisher fluid (Halon) which combines a high density and low absolute viscosity to achieve very low kinematic viscosity, actually less than liquid hydrogen [10]. Details of the flow loop are provided in [11].

Figure 5 illustrates the test apparatus. The test fluid enters the center and discharges axially across the two test seals. Seal inserts are pressed into cylindrical seats in the housing. The rotor segments of the seal are mounted eccentrically in the rotor with an eccentricity A. Hence, rotor rotation generates a synchronously-precessing pressure field. Axially-spaced, strain-gauge, pressure transducers are provided to measure the transient pressure field. Capacitance-type proximity probes are provided to simultaneously measure the rotor motion X(t), Y(t) relatives to the housing. The transient pressure measurements are integrated to define F_r/A and F_θ/A, the force coefficients parallel and normal to the seal eccentricity vector. In any test, five to ten cycles of data, containing on the order of 2,000 data points, are analyzed, yielding a calculated average and standard deviation for F_r/A and F_θ/A. The test results reported here were carried out to provide answers for the following questions:

(a) How do predictions from the current theory compare to test results?

(b) For damper seal configurations, (rough-stator/smooth-rotor) how do various roughness treatments compare in terms of leakage, stiffness, and damping?

Stator Configurations

Tests were carried out on the following stator configurations:

(a) smooth finish,

(b) knurled-indentation roughness,

(c) diamond-grid post pattern,

(d) round-hole pattern.

All seals use the same radial clearance, C_r = .527 mm. Seals b through d are illustrated in figures 6. The knurled-indentation roughness pattern is the same as that used in current test versions of the HPOTP (High Pressure Oxygen Turbopump), and the seal insert was supplied by Rocketdyne division of Rockwell International, the manufacturer of the SSME. The diamond-grid post pattern was manufactured by a milling operation which produced grooves which left the square post pattern. The round-hole pattern was also produced by a right-hand milling operation.

Empirical Turbulence Coefficients

With reference to the adequacy of current analysis, the stator and rotor roughness is characterized in terms of empirical coefficients. These coefficients must be calculated from the static test data before a theoretical prediction can be made for F_r/A and F_θ/A, and calculation of these coefficients is the subject of this subsection.

In the apparatus of figure 5, a smooth-seal insert is used in the left-hand side, while the damper-seal stators were inserted in the right hand side of the housing. To the extent possible, the same "very-smooth" finish was provided for both the smooth-seal insert and the rotor. Leakage rates and pressure gradients were measured for both the smooth and damper seals for all dynamic tests.

The steady-state axial pressure gradient equation has the form

$$-\frac{\partial p}{\partial z} = \sigma \left(\frac{\rho \bar{V}^2}{2}\right)$$

Hence, with a measured pressure gradient and a known density ρ and axial velocity $\bar{V}$, the parameter σ can be calculated. σ is related to the friction-factor coefficient λ by

$$\sigma = \lambda \left(\frac{L}{\bar{C}}\right)$$

The smooth-rotor/smooth-stator data were used to calculate σ_r and λ_r values which were assumed to apply for both the rotor and smooth stator. From the λ_r versus ω and R_{ao} data, the empirical coefficients mr, nr of the following friction-factor formula are calculated

$$\lambda_r = nr\, R_{ao}^{mr} \left[1 + (R\omega/\bar{V})^2\right]^{\frac{mr+1}{2}} \tag{36}$$

on a least-square basis, yielding

$$nr = 0.0674, \qquad mr = -0.217$$

For the smooth-rotor/rough-stator combinations, a combined σ_c is measured, which is related to the corresponding rotor σ_r and (rough) stator σ_s by

$$\sigma_c = \frac{\sigma_r + \sigma_s}{2} \Rightarrow \sigma_s = 2\sigma_c - \sigma_r \tag{37}$$

This formula was used to calculate σ_s for the rough stators by using measured values for σ_c and calculating a value for σ_r from Eq. (36) with the parameters of Eq. (37). The empirical coefficients obtained for the stator inserts are provided in table 1, together with an estimate of the relative-roughness parameter corresponding to pipe-friction data. The results are generally consistent with expectations, except for the positive value for ms obtained for the hole-pattern stator; however, over the Reynolds-number range tested, the combined friction-factor λ_c actually increased (slightly) with increasing R_{ao} for this stator insert.

Dynamic Test Data

For a given seal configuration, a test matrix is obtained by varying the axial Reynolds number and running speed. The R_{ao} range varies between the maximum flow capacity of the supply pump and the minimum ΔP sufficient to generate reasonable transient pressure signal amplitudes. For a given R_{ao} value, the running speed is varied sequentially over the running-speed capacity of the drive motors. Figures 7 through 10 illustrate theoretical and experimental results for the four stators tested. An inspection of these results demonstrates "reasonable" agreement between theory and experiment for F_θ/A but much larger F_r/A magnitudes at lower speeds than predicted. Further, the magnitude of F_r/A decreases more rapidly with increasing running speed than predicted.

DISCUSSION OF EXPERIMENTAL RESULTS

Comparison to Theory

If a circular orbit of the form

$$X = A\cos\omega t \qquad Y = A\sin\omega t$$

is assumed, Eq. (1) yields the following definition of force coefficients

$$F_r/A = -K - c\omega + M\omega^2$$

$$F_\theta/A = k - C\omega$$

where the cross-coupled mass coefficient m has been dropped as being negligible in comparison to the influence of k and C. At first glance, these equations suggest that sufficient independent equations could be obtained, in the present apparatus, to independently calculate all the rotordynamic coefficients by holding the flowrate constant and running at three different speeds. However, the fact that the coefficients depend on ω precludes this approach. While K, C, and M are weak functions of ω through their dependence on σ, the "cross-coupled" coefficients k and c are linear functions of ω. In fact, if the fluid is prerotated prior to entering the seal such that the inlet tangential velocity is $U_{\theta o}(o) = R\omega/2$, then theory predicts that $k = C\omega/2$, $c = M\omega$, and

$$F_r/A = -K, \quad F_\theta/A = -C\omega/2$$

The present test apparatus provides no intentional prerotation, and the expected result is of the form

$$k = b_1 C\omega/2, \quad b_1 < 1$$

$$c = b_2 M\omega, \quad b_2 < 1$$

$$F_\theta/A \cong -C_{ef}\omega = -C(1-b_1/2)\omega$$

$$F_r/A \cong -K_{ef} + M_{ef}\omega^2 = -K + M(1-b_2)\omega^2$$

The term C_{ef} denotes the "net damping coefficient" resulting from the drag force $C\omega A$ and the forward whirl excitation force kA. A direct comparison between theory and experiment is obtained by curvefitting the theoretical and experimental results for the F_r/A and F_θ/A to obtain predictions for K_{ef}, C_{ef}, and M_{ef}. Note that the procedure of curvefitting the data with respect to ω eliminates the running-speed dependency. Further, K_{ef} is the zero-running speed intercept of the F_r/A versus ω curve, and C_{ef} is the slope of the F_θ/A versus ω curve.

A comparison of measured and experimentally-derived values for K_{ef}, C_{ef}, and M_{ef} are given in table 2 for the stators tested, and support the following general conclusions:

(a) Direct stiffness values are substantially underpredicted by theory. This result is consistent with earlier water test results [5, 12]. Improved correlation generally results at larger $\bar{C}/R$ ratios.

(b) Net damping coefficients are overestimated by theory, but the agreement is reasonable and generally improves with increasing R_{ao}.

(c) The added-mass coefficient is substantially underpredicted by theory. However, this result is at variance with earlier water-test results [12] which show an overestimation of the added-mass coefficient.

Relative Performance of Stators

Dynamic Coefficients

Figures 11 and 12 illustrate K_{ef} and C_{ef} for the stators tested versus ΔP, and can be used for direct comparison of the stiffness and effective damping of the roughness designs. The results support the following conclusions.

(a) The knurled-indentation and the diamond-grid stators are, respectively, the most and least stiff. The hole-pattern and smooth stators have comparable stiffness.

(b) The hole-pattern and diamond-grid stators provide, respectively, the most and least net damping. The smooth and knurled-indentation stators have comparable net damping coefficients.

The disappointing performance of the diamond-grid stator is related to its larger average clearance. The relieving operation which yields the posts yields an average clearance of 0.889 mm as compared to the 0.527 mm minimum clearances of the remaining configurations.

Leakage Performance

To evaluate leakage performance, C_L is defined using the conventional discharge coefficient C_d definition

$$\Delta P = C_d \frac{\rho \bar{V}^2}{2}$$

which yields

$$\dot{Q} = 2\ R\overline{CV} = \left(\frac{\overline{C}}{R}\right) C_d^{-\frac{1}{2}} \cdot 2\pi R^2 \sqrt{\frac{2\Delta P}{\rho}} = C_L \cdot 2\pi R^2 \sqrt{\frac{2\Delta P}{\rho}}$$

Hence,

$$C_L = \left(\frac{\overline{C}}{R}\right) C_d^{-\frac{1}{2}} = \dot{Q}\Big/\left(2\pi R^2 \sqrt{\frac{2\Delta P}{\rho}}\right)$$

The coefficient C_L is a nondimensional relative measure of the leakage to be expected through seals having the same radius. Figure 13 illustrates C_L versus ΔP for the seal stators and demonstrates that the round-hole pattern and smooth stators have, respectively, the best and worst performance. The knurled-indentation pattern has a slightly better leakage performance than the diamond-grid pattern.

CLOSURE

A theory is presented, based on a simple modification of Hirs' turbulent lubrication equations, to account for different but directionally-homogeneous surface roughness treatments for the rotor and stator of annular seals. The theoretical results agree with von Pragenau's predictions that a "damper seal" which uses a smooth rotor and a rough stator yields more net damping than a conventional seal which has the same roughness for both the rotor and stator.

Experimental results for four stators confirm that properly-designed roughened stators can yield higher net damping values and substantially less leakage than seals with smooth surfaces. The best seal from both damping and leakage viewpoints uses a round-hole-pattern stator. Initial results for this stator suggest that, within limits, seals can be designed to yield specified ratios of stiffness to damping. Additional testing for this type of seal is scheduled for 1984-1985 to examine the influence of hole depth, hole shape, and the ratio of hole-relieved area to total surface area.

APPENDIX A: PERTURBATION COEFFICIENTS

$$B_s a_{0s} = \left[1 + (u_{\theta 0}/bu_{Z0})^2\right]^{\frac{ms+1}{2}}, \quad B_s = \left(1 + \frac{1}{4b^2}\right)^{\frac{ms+1}{2}}$$

$$B_r a_{0r} = \left\{1 + \left[(u_{\theta 0}-1)/bu_{Z0}\right]^2\right\}^{\frac{mr+1}{2}}, \quad B_r = \left(1 + \frac{1}{4b^2}\right)^{\frac{mr+1}{2}}$$

$$B_s a_{1s} = \left[1 + (u_{\theta 0}/bu_{Z0})^2\right]^{\frac{ms-1}{2}}$$

$$B_r a_{1r} = \left\{1 + \left[(u_{\theta 0}-1)/bu_{Z0}\right]^2\right\}^{\frac{mr-1}{2}}$$

$$A_{1z} = \left[a_{0s}\sigma_s(1-ms) + a_{0r}\sigma_r(1-mr)\right] /2f^4$$

$$A_{2z} = \left[(ms+1)\sigma_s a_{1s}u_{\theta 0} + (mr+1)\sigma_r a_{1r}(u_{\theta 0}-1)\right] /2b^2 f$$

$$A_{3z} = \left[a_{0s}\sigma_s(2+ms) + a_{0r}\sigma_r(2+mr)\right] /2f^2 + 2q/f^2$$

$$- \left[a_{1s}\sigma_s(1+ms)u_{\theta 0}{}^2 + a_{1r}\sigma_r(1+mr)(u_{\theta 0}-1)^2\right] /2b^2$$

$$A_{1\theta} = \left[\sigma_s a_{0s}u_{\theta 0}(1-ms) + \sigma_r a_{0r}(u_{\theta 0}-1)\ (1-mr)\right] /2f^3$$

$$A_{2\theta} = (\sigma_s a_{0s} + \sigma_r a_{0r})/2f^2$$

$$+ \left[\sigma_s(1+ms)a_{1s}u_{\theta 0}^2 + \sigma_r(1+mr)a_{1r}(u_{\theta 0}-1)^2\right] /2b^2$$

$$A_{3\theta} = \left[\sigma_s ms\ a_{os}u_{\theta 0} + \sigma_r mra_{0r}(u_{\theta 0}-1)\right] /2f$$

$$-f\left[\sigma_s a_{1s}(1+ms)u_{\theta 0}{}^3 + \sigma_r a_{1r}(1+mr)(u_{\theta 0}-1)^3\right] /2b^2$$

REFERENCES

1. Lomakin, A., "Calculation of Critical Speed and Securing of the Dynamic Stability of the Rotor of Hydraulic High Pressure Machines with Reference to Forces Arising in Seal Gaps," Energomashinostroenie, Vol. 4, 1958.

2. Allaire, P. E., Gunter, E. J., Lee, C.P., and Barrett, L. E., "The Dynamic Analysis of the Space Shuttle Main Engine High Pressure Fuel Turbopump Final Report, Part II, Load Capacity and Hybrid Coefficients for Turbulent Interstage Seals," University of Virginia Report UVA/528140/ME76/103, September 1976.

3. Black, H. F., and Jenssen, D. N., "Dynamic Hybrid Properties of Annular Pressure Seals," Proc. J. Mechanical Engineering, Vol. 184. pp. 92-100, 1970.

4. Childs, D. W., "Finite-Length Solutions for Rotordynamic Coefficients of Turbulent Annular Seals," ASME Trans. J. of Lubrication Technology, Vol. 105, pp. 437-444, July 1983.

5. Childs, D. W., "Finite-Length Solutions for the Rotordynamic Coefficients of Constant-Clearance and Convergent-Tapered Annular Seals," submitted for Third International Conference on Vibrations in Rotating Machinery, York, England, September 1984.

6. Von Pragenau, G. L., "Damping Seals for Turbomachinery," NASA Technical Paper 1987, 1982.

7. Hirs, G. G., "A Bulk-Flow Theory for Turbulence in Lubricant Films," ASME Trans. J. of Lubrication Technology. pp. 137-146, April 1973.

8. Fleming, D. P., "High Stiffness Seals for Rotor Critical Speed Control," ASME Paper 77-DET-10, Design Engineering Technical Conference, Chicago, Ill, 26-30 September 1977.

9. Yamada, Y., "Resistance of Flow through an Annulus with an Inner Rotating Cylinder," Bull. J.S.M.E., Vol. 5, No. 18, pp. 302-310, 1962.

10. Stephen, H. and Lucus, K., Viscosity of Dense Fluids, Plenum Press, New York - London, p. 59.

11. Childs, D., Nelson, C., Noyes, T., and Dressman, J. B., "A High-Reynolds-Number Test Facility: Facility Description and Preliminary Data," NASA Conference Publication 2250, Proceedings Workshop on Rotordynamic Instability Problems in High-Performance Turbomachinery - 1982, held at Texas A&M University, 10-12 May 1982.

12. Childs, D., and Dressman, J., "Convergent-Tapered Annular Seals: analysis and Testing for Rotordynamic Coefficients," accepted for publication ASME Trans. J. of Lubrication Technology.

TABLE I. - EMPIRICAL TURBULENCE COEFFICIENTS MS, NS,
AND ESTIMATES FOR RELATIVE ROUGHNESS

	ms	ns	$\hat{\varepsilon} = \hat{e}/2\bar{C}$
Smooth	-.240	.0989	.00069
Knurled-Indentation	-.136	.0697	.022
Diamond-Grid	-.0350	.118	.460
Hole Pattern	.0190	.0150	.058

TABLE II. - A COMPARISON OF THEORETICAL AND MEASURED VALUES FOR EFFECTIVE STIFFNESS, DAMPING AND ADDED-MASS COEFFICIENTS

SEAL	R_{ao}	$\frac{KEF_{ex}}{KEF_{th}}$	$\frac{CEF_{ex}}{CEF_{th}}$	$\frac{MEF_{ex}}{MEF_{th}}$
Smooth	120,100	2.182	0.6636	1.38
	170,600	2.216	0.6900	1.38
	270,500	1.297	0.7567	4.45
	385,200	1.142	0.9350	6.88
	495,700	1.261	0.9964	9.35
	500,900	1.478	0.9401	0.986
Knurled-Indentation	115,700	1.630	0.5613	4.24
	160,200	1.598	0.8166	3.82
	335,600	1.678	0.9836	18.6
	350,500	1.664	1.027	11.2
	368,200	1.706	1.041	4.23
Diamond Grid	115,100	1.745	0.4265	1.88
	159,800	1.310	0.4795	2.61
	335,600	1.065	0.9954	7.58
	349,900	0.8026	0.9583	11.9
	384,000	1.128	1.012	4.83
Hole Pattern	89,410	1.573	0.4506	1.94
	130,400	1.768	0.6997	2.25
	159,700	1.876	0.7867	2.58
	328,400	2.175	1.205	1.88

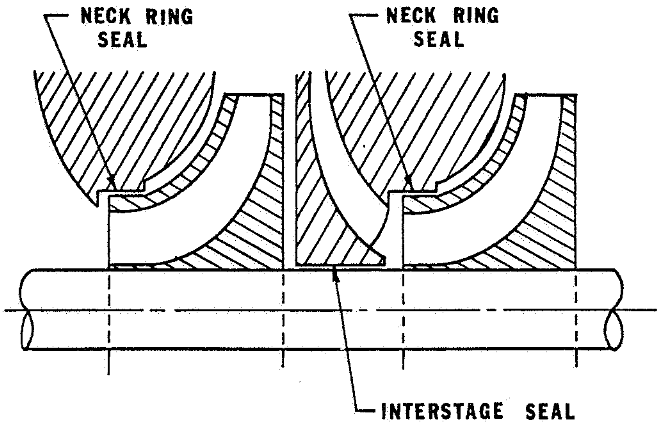

Figure 1. Neck-ring and interstage seals.

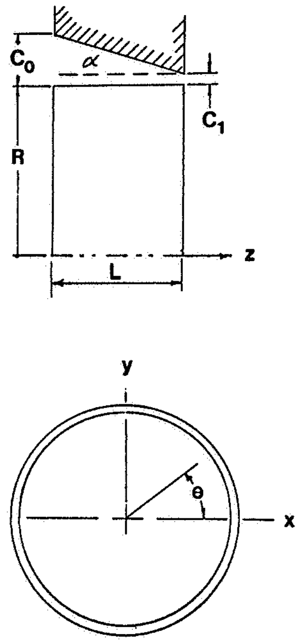

Figure 3. Tapered seal geometry.

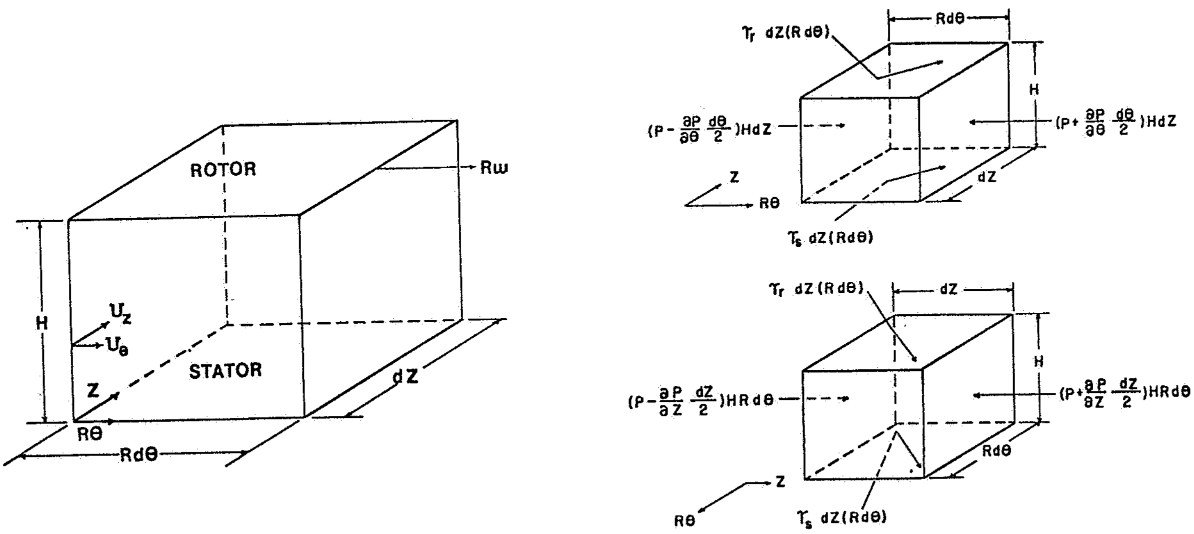

Figure 2. Seal differential element.

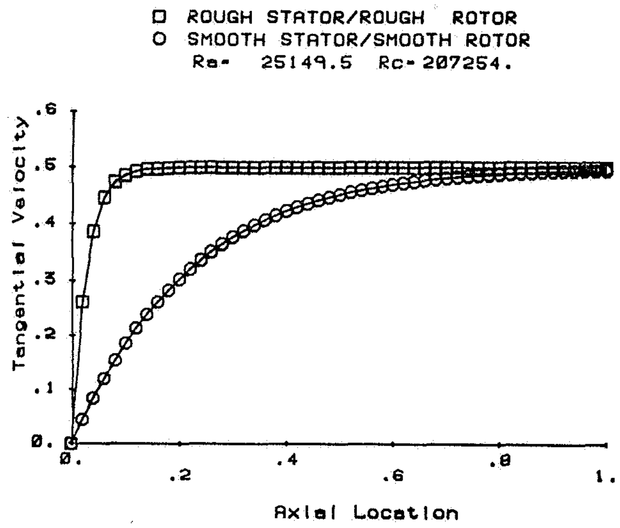

Figure 4(a). Predicted circumferential velocity development for the same rotor and stator roughnesses.

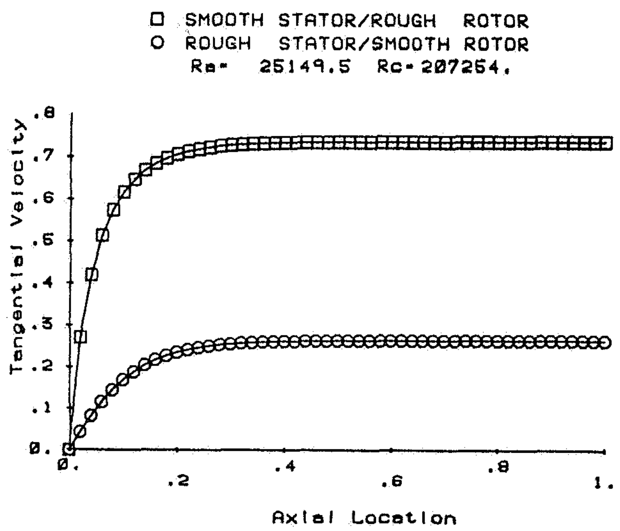

Figure 4(b). Predicted circumferential velocity development for different rotor and stator roughnesses.

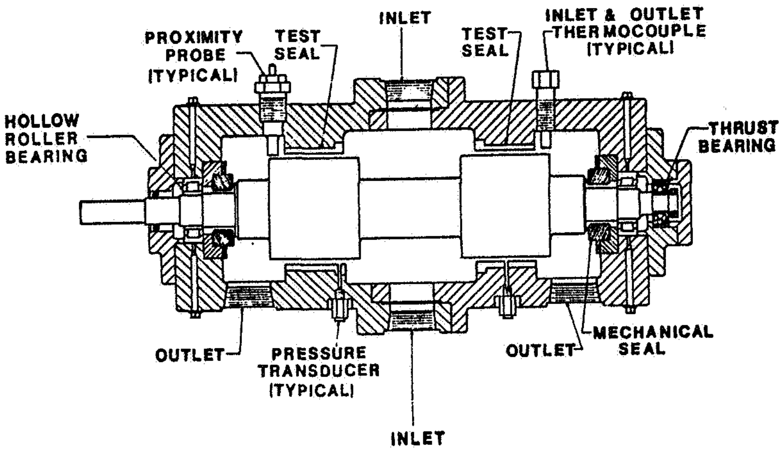

Figure 5. Test apparatus.

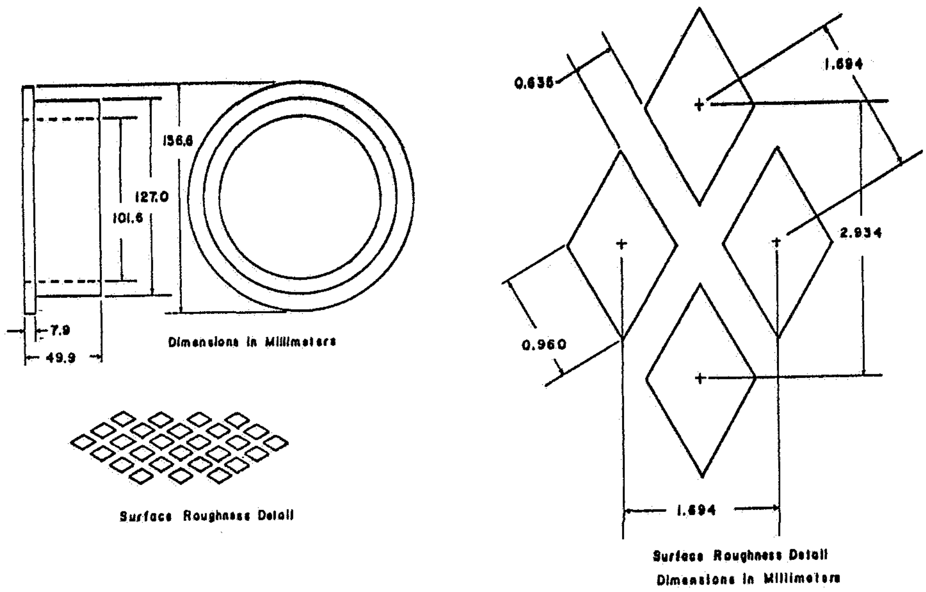

Figure 6(a). Rocketdyne-manufactured, knurled-indentation stator insert.

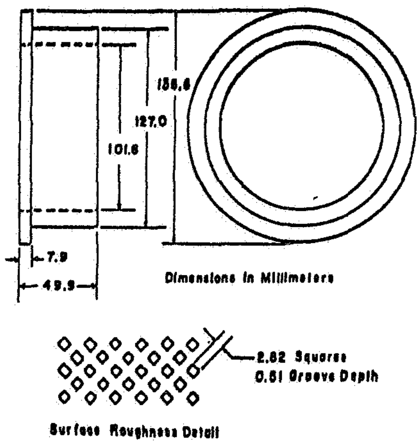

Figure 6(b). Diamond grid, post-roughness stator insert.

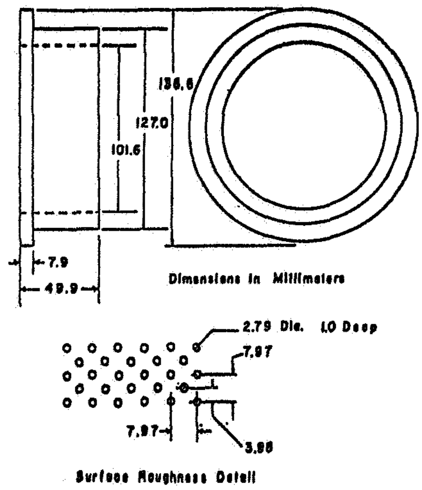

Figure 6(c). Round-hole pattern stator insert.

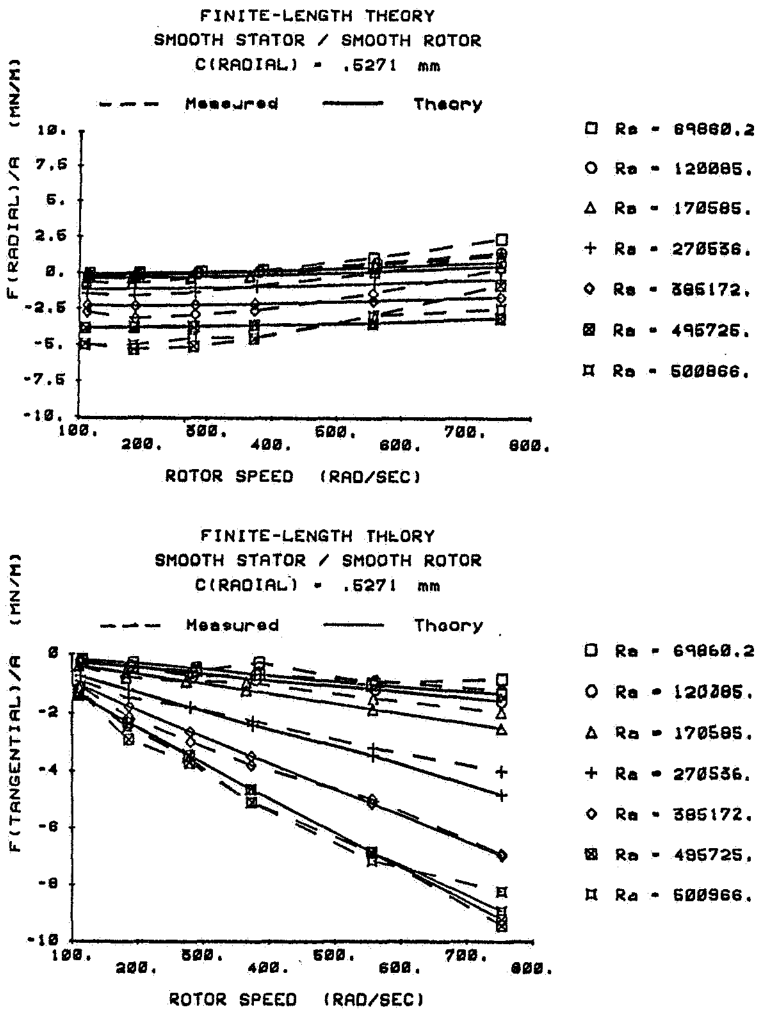

Figure 7.
Measured and theoretical results for F_r/A and F_θ/A; smooth stator.

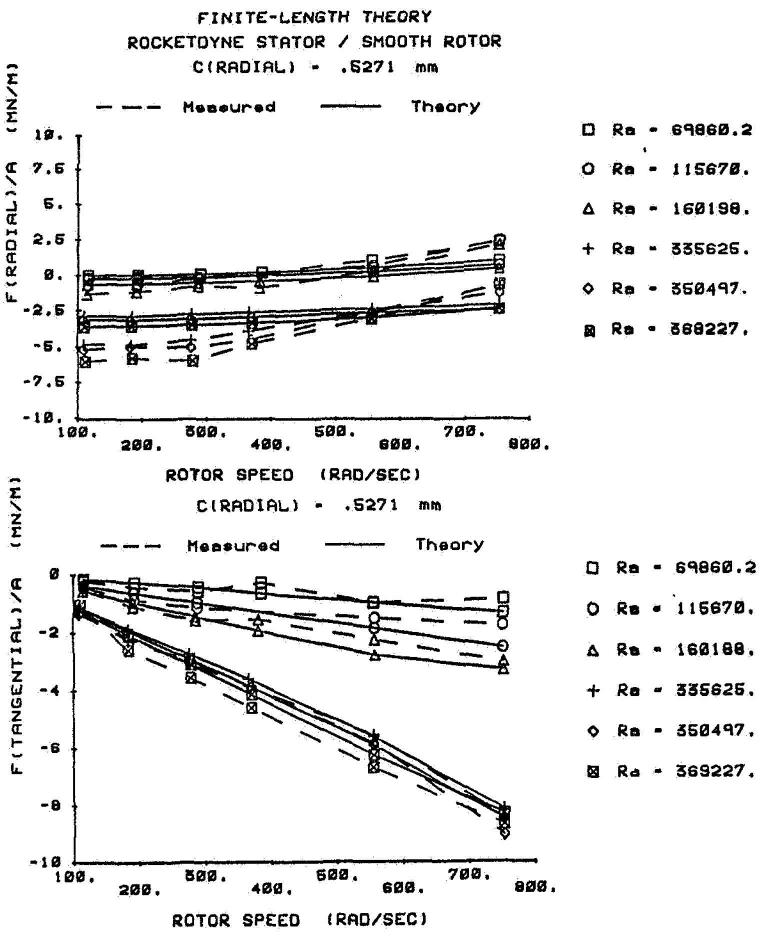

Figure 8.
Measured and theoretical results for F_r/A and F_θ/A; knurled-indentation stator.

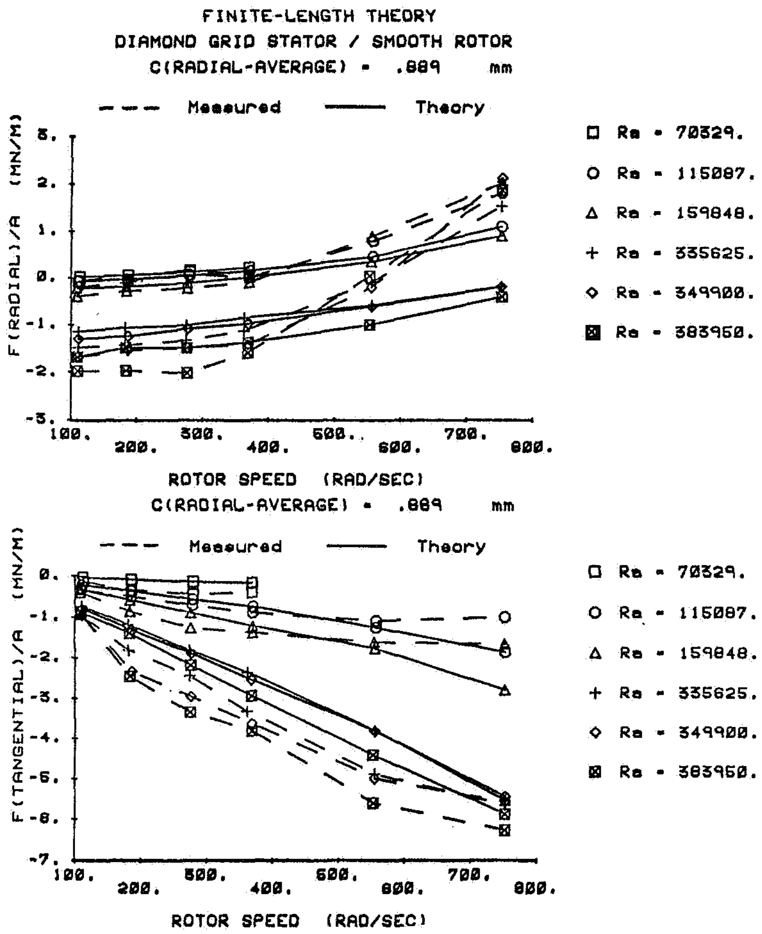

Figure 9.
Measured and theoretical results for F_r/A and F_θ/A; diamond-grid stator.

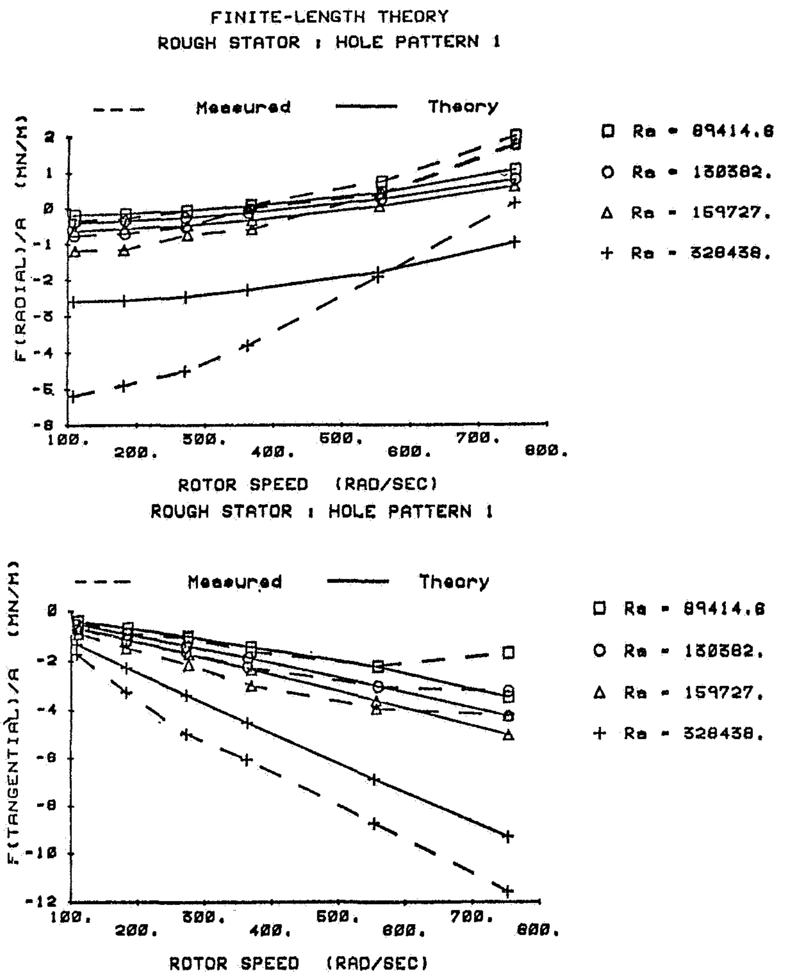

Figure 10. Measured and theoretical results for F_r/A and F_θ/A; round-hole pattern.

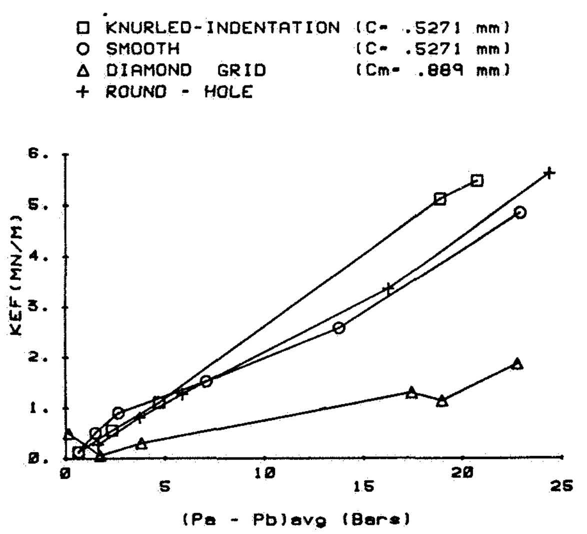

Figure 11. K_{ef} versus ΔP for stator inserts.

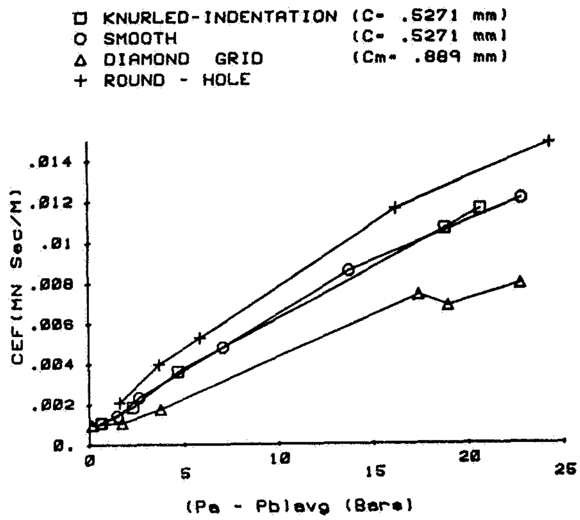

Figure 12. C_{ef} versus ΔP for stator inserts.

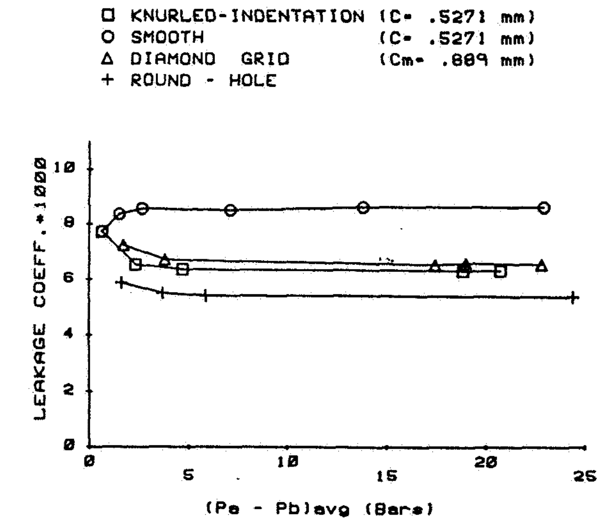

Figure 13. C_L versus ΔP for stator inserts.